SUBMITTED TO THE ASTROPHYSICAL JOURNAL
Preprint typeset using LATEX style emulateapj v. 11/10/09

ASYMMETRY AND THE NUCLEOSYNTHETIC SIGNATURE OF NEARLY EDGE-LIT DETONATION IN WHITE DWARF CORES

DAVID A. CHAMULAK[1,7], CASEY A. MEAKIN[2,3], IVO R. SEITENZAHL[4], JAMES W. TRURAN[1,5,6,7]

Draft version March 17, 2011

ABSTRACT

Most of the leading explosion scenarios for Type Ia supernovae involve the nuclear incineration of a white dwarf star through a detonation wave. Several scenarios have been proposed as to how this detonation may actually occur, but the exact mechanism and environment in which it takes place remain unknown. We explore the effects of an off-center initiated detonation on the spatial distribution of the nucleosynthetic yield products in a toy model – a pre-expanded near Chandrasekhar-mass white dwarf. We find that a single near edge-lit detonation results in asymmetries in the density and thermal profiles, notably the expansion timescale, throughout the supernova. We demonstrate that this asymmetry of the thermodynamic trajectories should be common to off-center detonations where a small amount of the star is burned prior to detonation. The asymmetry stems from the fact that in one hemisphere the propagation direction of the detonation wave is largely in the direction of final (radial) expansion, whereas in the other hemisphere it is largely opposing it. The sensitivity of the yields on the expansion timescale results in an asymmetric distribution of the elements synthesized as reaction products. We tabulate the shift in the center of mass of the various elements produced and find an odd-even pattern for elements past silicon. We find a clear compositional asymmetry, in coordinate as well as in velocity space, in regions of the white dwarf that do not burn to nuclear statistical equilibrium.

Subject headings: nuclear reactions, nucleosynthesis, abundances — supernovae: general — white dwarfs

1. INTRODUCTION

The fact that their peak absolute magnitude is correlated with the width of the light curve has allowed Type Ia supernovae (SNe Ia) to be used as standard candles in determining cosmological distances. Despite this widespread use of SNe Ia as standard candles, many problems in describing how the explosion of the star happens still remain.

Two promising candidates for an explosion mechanism are the sub-Chandrasekhar double detonation model (Woosley & Weaver 1994; Fink et al. 2010) and the gravitational confined detonation (GCD) model (Plewa et al. 2004). In both models, most if not all of the nuclear burning occurs in a detonation wave. In the sub-Chandrasekhar model a layer of helium is deposited on the surface of a white dwarf. The helium layer detonates resulting in a shock wave traveling around the surface of the white dwarf. When the shock wave converges at the antipode, a detonation is thought to be triggered at the edge of the carbon-oxygen core (Woosley & Weaver 1994; Fink et al. 2010; Sim et al. 2010; Kromer et al. 2010). The nucleosynthetic yield is set predominantly by the mass of the carbon-oxygen white dwarf core and the mass of the helium layer (Woosley & Weaver 1994; Fink et al. 2010).

In the GCD model, the carbon burning runaway within the convective core of a near Chandrasekhar-mass WD is postulated to occur in a small region displaced from the stellar center that becomes a highly buoyant flame bubble and quickly rises to the stellar surface after burning only a few percent of the star during its ascent (e.g. Livne et al. 2005). When the buoyant ash, as well as unburned material pushed ahead of the rising flame bubble, erupts forth from the stellar core it is largely confined to the surface of the white dwarf by gravity. It then becomes a strong surface flow that sweeps completely over the star, eventually converging in a region opposite to the breakout location. The high temperatures and densities reached within the converging surface flow are thought to trigger a detonation (Seitenzahl et al. 2009a,b) which incinerates the mostly unburned carbon-oxygen white dwarf (Meakin et al. 2009).

The resulting nucleosynthetic yield consists almost entirely of detonation burning products and depends on how much the star has expanded by the time the detonation initiates. More highly expanded (hence lower density) cores at detonation result in a smaller fraction of Fe peak nuclei, less ^{56}Ni, and consequently a larger fraction of intermediate mass elements (IMEs) due to incomplete relaxation to nuclear statistical equilibrium (NSE). Therefore, lower luminosity (less ^{56}Ni producing) explosions are accompanied by a larger yield of IMEs (see e.g. Mazzali et al. 2007).

The expansion of the star prior to detonation is a result of the work done on the star by the rising flame bubble. Deflagrations that burn more mass prior to reaching the stellar surface excite higher amplitude pulsations and hence more-expanded stars at the time of detonation. It has been found that the expansion of the star due to the deflagration is very well represented by the fundamental radial pulsation mode of the underlying white dwarf (see Fig. 2 and Fig. 12 in Meakin et al. 2009). Therefore, while it is essential to understand the nature of the deflagration so as to better understand the mapping between initial conditions and final outcomes, the range of outcomes due to the deflagration can be parameterized by the pulsation amplitude, resulting in a one parame-

dchamulak@anl.gov
[1] Physics Division, Argonne National Laboratory, Argonne, IL
[2] Theoretical Division, Los Alamos National Laboratory, Los Alamos, NM
[3] Steward Observatory, University of Arizona, Tucson, AZ
[4] Max Planck Institute for Astrophysics, Garching, Germany
[5] Department of Astronomy and Astrophysics, University of Chicago, Chicago, IL
[6] Center for Astrophysical Thermonuclear Flashes, University of Chicago, Chicago, IL
[7] Joint Institute for Nuclear Astrophysics

ter family of models. While the phase of the pulsation at the time of detonation is an additional parameter, it plays a lesser role since the pulsation period is longer then the detonation crossing time.

In this Paper we explore the nucleosynthetic yields that result from an edge-lit detonation of a pre-expanded near Chandrasekhar-mass white dwarf core out of hydrostatic equilibrium. This is a toy-model which neglects the effect the deflagration has on the nucleosynthesis. However, due to the small amount of mass burned in the deflagration it captures most of the essential features of the GCD model. The physical mechanism that gives rise to the abundance asymmetries in the ejecta will furthermore manifest itself in other off-center detonation models, such as the sub-Chandrasekhar double detonation models.

In Section 2 we describe the explosion model and our computational method. Section 3 is comprised of three parts. First, we discuss how the dynamics of an asymmetric detonation affect the hydrodynamic profile of the SN Ia remnant. We then consider how variations in the thermodynamic trajectories of detonated material affect the resulting nucleosynthesis. Finally, we present the elemental yields found for our explosion model and quantify the asymmetric distribution thereof in terms of center of mass offsets, which we provide in tabulated form. We also show that there is an asymmetric distribution in velocity space for elemental nickel. We then conclude in Section 4, with a discussion of how our results relate to previous work and how our work can be improved.

2. THE EXPLOSION MODEL

In the explosion model discussed in this paper, we initiate a detonation in the surface layer of a cold (T=4×10^7 K) white dwarf of mass $1.365 M_\odot$, comprised of 50% carbon and 50% oxygen by mass, which has been expanded according to its fundamental radial-pulsation mode by such an amplitude that it has a central density of $10^8\ \mathrm{g\,cm^{-3}}$. This expansion results in $\sim 1 M_\odot$ of high density material ($\rho > 10^7\ \mathrm{g\,cm^{-3}}$), that burns to NSE in the detonation (primarily as ^{56}Ni). The remaining $\sim 0.37 M_\odot$ of material burns to IMEs, e.g. Si, S, Ca, and Ar, resulting in only a small amount ($< 0.04 M_\odot$) of unburned C/O in the outermost layers of the remnant. The detonation is initiated by heating a small spherical volume (~ 4 km in radius) within the surface layer of the expanded white dwarf where the density is $10^7\ \mathrm{g\,cm^{-3}}$. The reactive-hydrodynamic simulation of the explosion was conducted using the FLASH code (Fryxell et al. 2000). The code framework and the included physics is identical to that described in Meakin et al. (2009), and an effective adaptive mesh refinement resolution of 1 km is used. An in-depth description of the detonation phase, which results in a homologously expanding remnant, can be found in Meakin et al. (2009). Detailed yields are calculated by post processing Lagrangian tracer particles included in the explosion calculation and are the primary focus of this paper. We recorded the time history of $\sim 10^4$ particles that were initialized to sample evenly the initial mass of the white dwarf.

Our reaction network incorporates 493 nuclides from n to ^{86}Kr (Table 1). We use the reaction rates from the Joint Institute for Nuclear Astrophysics REACLIB Database[8] (Cyburt et al. 2010, and references therein); the light-element rates are mostly experimental and are from compilations such as Caughlan & Fowler (1988) and Iliadis et al. (2001). Weak reaction rates are taken from Fuller et al. (1982) and Langanke & Martínez-Pinedo (2001). Screening is incorporated using the formalism of Graboske et al. (1973).

[8] http://groups.nscl.msu.edu/jina/reaclib/db/

TABLE 1
493-NUCLIDE REACTION NETWORK

El.	*A*	El.	*A*	El.	*A*	El.	*A*
n							
H	1–3	Ne	17–28	K	35–46	Ni	50–73
He	3–4	Na	20–31	Ca	35–53	Cu	54–70
Li	6–8	Mg	20–33	Sc	40–53	Zn	55–72
Be	7, 9–11	Al	22–35	Ti	39–55	Ga	58–73
B	8, 10-14	Si	22–38	V	43–57	Ge	59–76
C	9–16	P	26–40	Cr	43–60	As	62–76
N	12–20	S	27–42	Mn	46–63	Se	62–82
O	13–20	Cl	31–44	Fe	46–66	Br	71–81
F	15–24	Ar	31–47	Co	50–67	Kr	71–86

3. RESULTS

3.1. *Explosion Dynamics and Remnant Asymmetry*

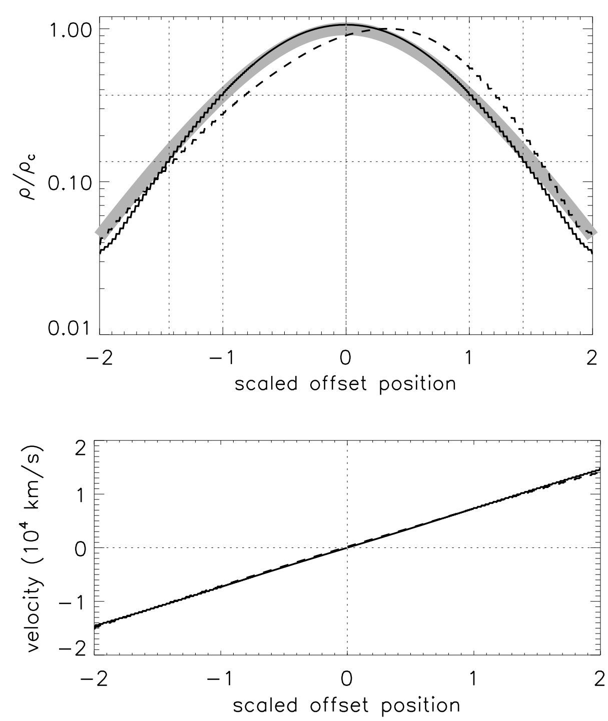

FIG. 1.— Late time (t > 3 s) density and velocity profiles for post-detonation state. The density is scaled by the peak value and the position is scaled by the density e-folding distance (5.6×10^7 cm and 1.25×10^8 cm pre and post-detonation, respectively) the equatorial direction . The thick gray line shows the scaled density profile of the initial WD model, while the post-detonation state model is shown by thick black lines for lines through the equator (solid) and through the poles (dashed).

The detonation propagates away form the point of initiation at nearly the Chapman–Jouguet (CJ) speed, $D_{CJ} \sim 1.2\times10^9\ \mathrm{cm\,s^{-1}}$ at a Mach number of $M_{CJ} \sim D_{CJ}/c_s \sim 3.4$. Because of the weak upstream density dependence of the detonation speed under these conditions, the detonation front remains very nearly spherical in shape as it engulfs the star. The total time required for its passage across the expanded

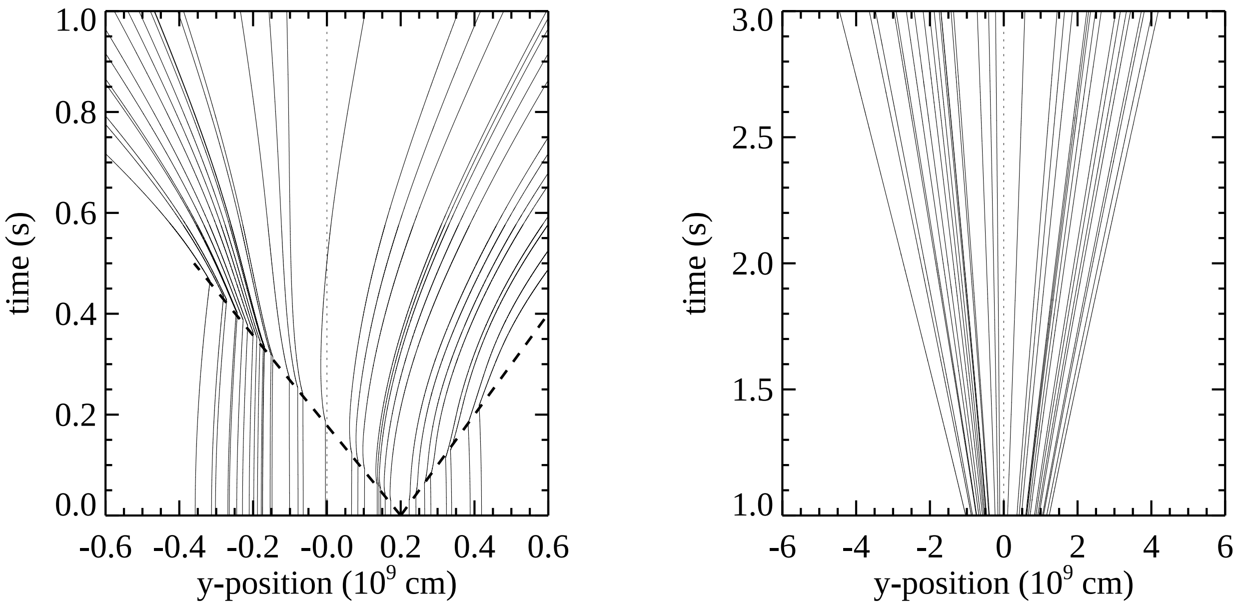

FIG. 2.— (left) On-axis Lagrangian tracer particle positions are shown as a function of time in this space-time diagram. The thick dashed line shows the theoretical position of a constant speed detonation originating from the location $y = 0.2 \times 10^9$ cm, coincident with the detonation initiated in the simulation. A theoretical detonation speed taken to be $v_{\rm det} = 1.1 \times 10^9$ cm s^{-1} for the detonation as it moves inward toward the high density core and a speed that is 10% lower as it moves outward into the low density surface material provides a very good match to the simulation data. (right) At times greater than 1s the Lagrangian tracer particles exhibit homologous expansion

white dwarf core is $t_{cross} \sim 2r/D_{CJ} \sim 0.5$ s. This is followed by a period of ~ 0.5 s in which the pressure forces drive the completely incinerated remnant into a homologous expansion, characterized by a purely radial expansion velocity profile with an expansion rate proportional to the radial position $v \propto r$. After only a few seconds, the remnant is expanding ballistically, and the total energy budget is dominated by the kinetic energy. The homologous velocity profile results in a self-similar density profile which persists until the remnant begins to interact with the interstellar medium.

The expanding remnant resulting from the detonation is marked by significant asymmetry. The late time density profiles along the symmetry axis and the equator are shown in Fig 1, scaled by the peak density in the remnant ρ_c. The initial, spherically symmetric white dwarf density profile is also shown for comparison. It can be seen that the density peak is shifted into the hemisphere in which the detonation was initiated, $y > 0$ in this case, resulting in a steeper density gradient in this hemisphere. This is in agreement with the series of GCD simulations described in Meakin et al. (2009)(see their Fig. 9 - 11) which show that the density isocontours in the remnant are well described by concentric circles that have centers offset from the initial stellar center. The density isocontours were found to have larger offsets at higher densities, with the largest offset centered on the peak density in the remnant. *In all cases the density peaks on the detonation side of the remnant and has a steeper density gradient in that region.*

Unlike the density profile, the velocity profile (also shown in Fig. 1) does not show an asymmetry, but is everywhere radially directed and spherically symmetric. This leads to an asymmetry in the density as a function of expansion velocity, which is likely to result in a viewing angle dependence for the light curve and the spectral signature. Related composition asymmetries, discussed in §§3.2 and 3.3 below, also contribute to observable asymmetries and viewing angle dependencies.

A revealing format for presenting the dynamics of the detonation and the subsequent expansion is the space-time diagram. In Fig. 2 we present the space-time trajectories for all of the tracer particles that were initialized near the symmetry axis of the white dwarf. The left panel shows the time period over which the detonation traverses the stellar core, while in the right panel we show the later time evolution that ends in a radially expanding, ballistic trajectory for each of the particles. The bold dashed line in the left panel shows the path taken by a theoretical detonation having a constant speed, which matches the kinks in the particle trajectories very well.

The following features in this figure merit further discussion. (1) The trajectories are slowly converging prior to detonation. This is the signature of the stellar core undergoing mild contraction as a result of having been expanded by a radial pulsation mode prior to detonation. (2) The detonation accelerates material in the direction it is propagating. This is the primary source of the asymmetry imprinted on the remnant at late times. The Lagrangian tracer particles in the detonated hemisphere are first accelerated towards the stellar center by the detonation before they are turned around by pressure forces and accelerated to their final, outwardly directed expansion velocities. On the other hand, tracers in the opposite hemisphere are accelerated by the detonation in the same direction as their final expansion velocity, reaching their final velocity on a shorter timescale. (3) The material in the detonated hemisphere is accelerated to lower velocities overall compared to material in the opposite hemisphere (see Fig. 2 (right)). This mapping between initial position (and therefore initial density) and resultant expansion velocity explains the density profile: the material lines in the more rapidly expanding hemisphere are stretched out over a larger region of space, and hence to a lower relative density, than the more slowly expanding regions. (4) A natural consequence of the explosion dynamics is an asymmetry in the expansion timescale t_{exp}, defined as the time required for the detonated material to drop from its post-detonation temperature maximum T_{max} to $e^{-1}T_{max}$, resulting from the differential rate at which material cools (nearly adiabatically) due to the post-detonation expansion. This follows directly from point (2) above. The expansion timescale asymmetry is shown in Fig. 3 where we have plotted the tracer particles at their initial position in the stellar core, color coded by their post-detonation expansion timescale. It is obvious from this figure that the material in the detonated hemisphere $(y > 0)$ has overall a higher expansion timescale than in the opposite hemisphere for a given initial upstream density. As will be discussed in §§3.2 and 3.3 this expansion timescale distribution imparts an asymmetry in the resultant nucleosynthetic yield.

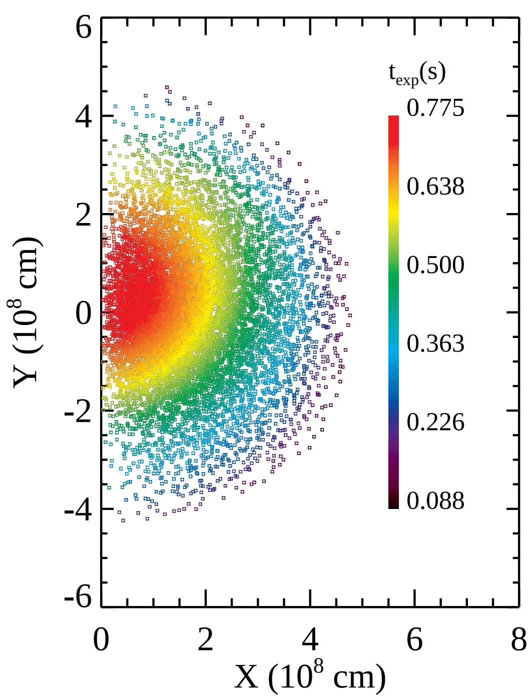

FIG. 3.— Initial spatial position of the tracer particles. Color represents each particle's expansion time scale. The center of the star is at X=0 Y=0 The detonation was initiated at X=0 Y=5. Particles on the side of the star where the detonation starts have higher expansion time scales then the particles on the opposite side of the star.

3.2. *Nucleosynthesis Dependence*

We find that nuclear burning in SNe Ia progresses in three distinct stages (Khokhlov 1983, 1991). The first stage is carbon burning. During carbon burning $^{12}C+^{12}C$ is the primary reaction taking place. We find that carbon burning never reaches an equilibrium state in a small region of the star where the final carbon mass fraction is above 10^{-4}. The carbon burning reactions are sensitive to temperature with

$$\frac{dY(^{12}\mathrm{C})}{dt} \propto f(T_9)T_9^{-2/3}e^{-84.165T_9^{-1/3}}. \qquad (1)$$

Here $dY(^{12}\mathrm{C})/dt$ is change in ^{12}C abundance over change in time, T_9 is temperature in units 10^9 K, and $f(T_9)$ is a function defining the temperature effect on the branching ratio between the $^{12}\mathrm{C}(^{12}\mathrm{C},\alpha)^{20}\mathrm{Ne}$ and $^{12}\mathrm{C}(^{12}\mathrm{C},p)^{23}\mathrm{Na}$ reaction (Caughlan & Fowler 1988). Any change in the thermal profile will result in a different abundance pattern for material that does not proceed to the next phase of burning.

The next stage is oxygen burning. Here ^{16}O and the products of carbon burning proceed to silicon group elements, like S, Ar, and Si. As in carbon burning, oxygen burning never reaches an equilibrium state and therefore also shows a dependence on the thermal history. We find $X(^{16}\mathrm{O}) > 10^{-5}$ if the next burning stage did not start. Very little mass of the star is in a region that does not complete either carbon or oxygen burning, so most of the star proceeds to the next burning stage.

At higher temperatures and densities, silicon burning is the dominant form of nucleosynthesis. In silicon burning groups of nuclides enter into equilibrium; a state known as quasi-statistical equilibrium (QSE; e.g., Woosley et al. 1973). There are two ways in which changing the expansion time scale can affect the abundances in QSE. First, while equilibrium holds within a group of nuclides, it does not hold between groups. Second, within a group of nuclides in equilibrium reactions freeze out at different temperatures, resulting in an abundance pattern that depends on the expansion time scale. This will be further explored below.

Fig. 4 shows how the abundances of silicon and nickel vary as functions of expansion time scale over a small range of temperatures for tracer particles that never finish silicon burning. Even with the scatter from plotting particles with different peak temperatures, there is a clear dependence of the abundances on expansion timescale. The directions of these trends are counterintuitive, but Fig. 5 shows their origin. Both tracer particles shown reach a peak temperature of $\sim 5\times10^9$ K, and their nucleosynthesis is nearly identical up to that point. The particle with the longer $(0.6016\ \mathrm{s})$ thermal expansion time scale, however, has a temperature that falls faster over the first 0.1 s than the particle with the shorter $(0.4428\ \mathrm{s})$ thermal expansion time scale. This rapid decrease in temperature results in less ^{28}Si burned to ^{56}Ni even though the thermal expansion time scale is longer.

Material exposed to high enough density and temperature conditions for long enough will arrive in a state of nuclear statistical equilibrium (NSE). In this state all nuclear reactions enter equilibrium and lose all history of the thermal evolution up to that point. For material that has reached this state, the only dependence that the final yield has on expansion timescale occurs during the process of freeze out. Freeze out occurs for a nuclide when the temperature drops low enough that all strong reactions become too slow to change the nuclides abundance again. Because this condition occurs at different temperatures for different nuclides, the final yield depends on the rate at which material cools. Like QSE different reactions freeze out at different temperatures, leading to yields that depend on the expansion timescale. Therefore, all three stages of burning and NSE in SNe Ia are affected by different expansion time scales, resulting in a clear compositional asymmetry that will be discussed in the following section.

3.3. *Phenomenology*

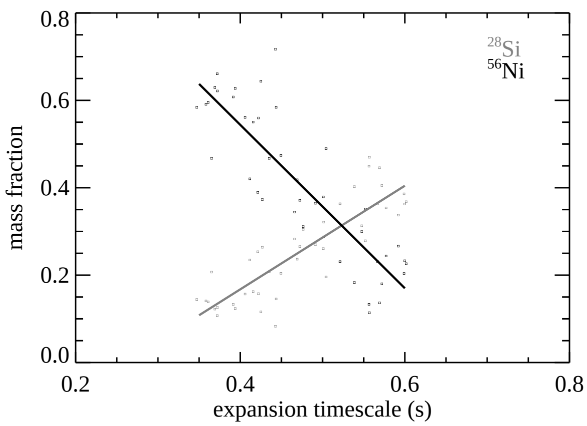

FIG. 4.— Mass fraction of ^{28}Si(red) and ^{58}Ni(blue) as a function of expansion time scale. This plot was made from tracer particles that had a maximum temperature between 4.99×10^{9} K and 5.01×10^{9} K and a density of approximately 1.5×10^{7} $\mathrm{g\,cm^{-3}}$.The lines shown are least squares fits to the data.

We now present the results of our reaction network calculations for a near edge-lit detonation in a SN Ia model. We find that a number of nuclides exhibit pronounced asymmetries across the stellar remnant. We quantify this effect by calculating the center of mass for a given element. Suppose a tracer particle i has a mass fraction $X_i(Z)$ of element Z, and its position is given by vector $\mathbf{r}_i$. Then the center of mass for a given element, $\mathbf{r}_{cm}(Z)$, is given by the equation

$$\mathbf{r}_{cm}(Z) = \left(\sum_i X_i(Z)\mathbf{r}_i\right) / \left(\sum_i X_i(Z)\right). \tag{2}$$

Due to the cylindrical symmetry of our explosion model the displacement of the center of mass for any element lies along the y axis. A velocity for the center of mass $\mathbf{v}_{cm}$ can be calculated by replacing $\mathbf{r}_i$ by the velocity $\mathbf{v}_i$ in equation 2. Table 2 shows the total mass and displacement of the center of mass for elements between carbon and germanium. For reference the detonation was initiated at $\sim 2\times10^{8}$ cm. These numbers are correct for the end of our simulation $(t\sim 3\text{ s})$ where strong reactions have frozen out and homologous expansion has been reached. Some of the isotopes making these elements, ^{56}Ni for example, decay so Table 2 evolves with time. Elements lighter than silicon have their masses distributed more in the direction where the detonation was initiated. Elements heaver than silicon are, for the most part, distributed away from where the detonation was initiated. These elements also display an odd-even pattern where odd Z nuclei are predominantly distributed farther away from the start of the detonation than their even Z counterparts.

Our simulation was not run sufficiently past freeze out to allow all beta unstable nuclei to decay. However, if we decay the unstable nuclei and group them in elemental abundances, we find Ni to have the greatest asymmetry over the star. In material not burned to equilibrium we find the abundance of elemental Ni between $+90^\circ$ and -90° latitude to increase by an order of magnitude. Figure 6 shows the dependence of elemental Ni on latitude.

An interesting side effect of the different expansion times is that material on opposite sides of the star expands at different velocities. This leads to a gradient in velocity space. Figure 7 shows how elemental Ni varies with radial velocity. In material not burned to equilibrium the part of the remnant with the most Ni is also the part with the highest radial velocity. This is self-consistent since the Ni abundance is greater on the side of the remnant with the shortest expansion time. Therefore, it follows it should have the highest radial velocity.

TABLE 2
CENTERS OF MASS AND VEOCITIES FOR VARIOUS ELEMENTS

	ΔCM (10^{8} cm)	Vcm ($10^{8}\mathrm{cm\,s^{-1}}$)	total mass (g)
C	29.1	9.9	9.00e+26
N	18.2	6.2	2.91e+22
O	7.30	2.4	7.28e+28
F	27.9	9.4	2.19e+19
Ne	28.7	9.9	1.03e+27
Na	25.6	8.8	1.12e+24
Mg	13.8	4.9	1.37e+28
Al	21.6	7.5	1.74e+25
Si	-1.09	-0.6	2.18e+29
P	-4.44	-1.9	8.34e+25
S	-2.68	-1.2	1.18e+29
Cl	-9.31	-3.7	1.82e+25
Ar	-2.95	-1.3	2.60e+28
K	-4.53	-1.7	5.12e+24
Ca	-2.55	-1.1	2.80e+28
Sc	-3.36	-1.3	2.02e+23
Ti	-2.78	-1.1	3.93e+25
V	-2.04	-0.7	3.68e+24
Cr	-2.37	-1.0	7.60e+26
Mn	-3.68	-1.4	2.58e+25
Fe	-1.80	-0.8	1.71e+28
Co	-5.59	-2.2	3.06e+26
Ni	0.00	0.0	2.16e+30
Cu	-3.06	-1.1	4.68e+27
Zn	0.17	0.1	2.93e+28
Ga	-2.09	-0.7	3.09e+25
Ge	-1.48	-0.5	6.31e+26

4. DISCUSSION

We have computed the abundances and spatial distributions of nuclides in an explosion of an expanded near Chandrasekhar-mass WD resulting from an off-center initiated detonation, a toy model that captures the key feature of some SN Ia explosion models. We find a compositional asymmetry in the ejecta produced by the detonation. This compositional asymmetry is connected with the thermal expansion time scale. The different expansion timescales also result in a compositional asymmetry in velocity space.

Our results are related to previous studies done on off center burning in SNe Ia. The 'toy model' constructed in Hillebrandt et al. (2007) and Sim et al. (2007) is very similar to our calculated results. Maeda et al. (2010) showed that expansion velocity gradients as inferred from the Si II λ6355 absorption feature could be explained by a velocity shift of $3500\ \mathrm{km\,s^{-1}}$ in Si happening in an 'opening angle' $105-110^\circ$ away from the ignition points. Our model has a similar effect with ^{28}Si having ejection velocities $\sim 10000\ \mathrm{km\,s^{-1}}$ faster on the side of the star opposite of the detonation. The ejecta in our model, however, do not have a sharp transition in velocity but a gradual increase in velocity starting at a point $\sim 90^\circ$ away from the ignition point. It is difficult to determine if our model can reproduce the observed velocity gradients. It is worth noting that the deflagration to detonation transition model used in (Maeda et al. 2010) did not produce the observed velocity shift or 'opening angle' either.

Our results can be improved in several ways. First, light

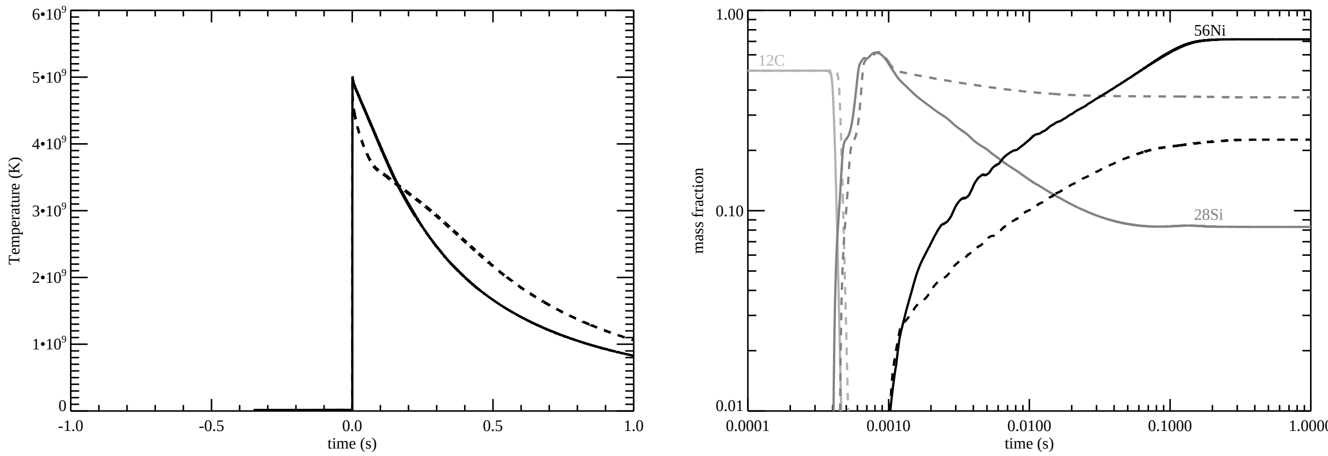

FIG. 5.— (left) Temperature profile for two particles with similar peak temperatures but different expansion time scales. The expansion time scale for the solid line is 0.4428 s and the expansion time scale for the dashed line is 0.6016 s. The times for both particles have been offset such that the peak temperature is reached at 1×10^{-3} s. (right) The mass fraction of ^{12}C, ^{28}Si, and ^{58}Ni as a function of time for the same time-adjusted particles.

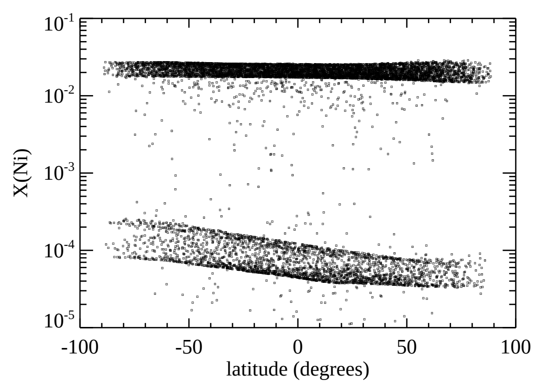

FIG. 6.— Final abundance of elemental Ni as a function of the ejection angle relative to the center of the star. The detonation started in the surface layer of the star in the theta = 90 direction. The particles with a Ni abundance above 10^{-4} are particles that have burned to NSE.

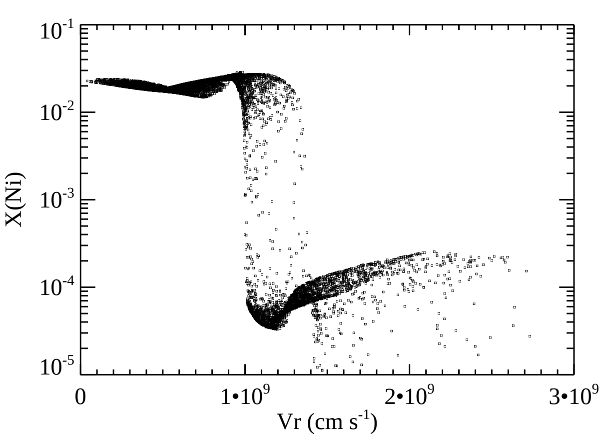

FIG. 7.— Final abundance of elemental Ni as a function of the final radial velocity. The particles with a Ni abundance above 10^{-4} are particles that have burned to NSE. Particles with a Ni abundance less than 10^{-5} show greater Ni abundance for larger radial velocities.

curves and spectra need to be generated to test the observational signature in more detail. It is currently unclear how much of an observation effect this asymmetry will have. A series of synthetic spectra generated over a range of time allows for direct comparison with observed supernovae.Kasen & Plewa (2005) attempted to calculate the spectral signatures of GCD by considering ejecta interacting with an extended atmosphere. The ejecta in their model were calculated from a 1-D model and therefore are spherically symmetric and lack compositional asymmetry. When revisiting the problem in 2-D the nucleosynthesis was done approximately and for only 13 elements (Kasen & Plewa 2007). We conjecture that even if compositional effects are obscured the spectra will show some dependence on observing angle, because the side of the remnant that expands at higher velocities will also be at a lower density making it more transparent at earlier times. The surface flow, which consists partly of deflagration ash, which was excluded from our present model, needs to be considered. The surface flow might also have a spectral signature itself such as the presence of an high-velocity calcium absorber (Kasen & Plewa 2005) and should be compared with the underlying compositional asymmetry. In the case of sub-Chandrasekhar models detonation of a pure helium shell leads to a layer containing iron-group elements such as titanium and chromium around the core ejecta (Fink et al. 2010; Sim et al. 2010; Kromer et al. 2010).

Second, we do not include the effects of metallicity on the nucleosynthesis. Our model is initially composed of ^{12}C and ^{16}O. However, it has been shown that prior to the explosion of a carbon-oxygen white dwarf in a SN Ia there is a long period during which some ^{12}C is converted into ^{13}C as well as heaver elements (Chamulak et al. 2008). This process makes even the most metal poor SNe Ia have a composition of more than ^{12}C and ^{16}O. It is worth mentioning that for deflagration–detonation transition (DDT) models where the detonation density was allowed to very in relation to the flame speed as a function of metallicity (Chamulak et al. 2007) the yield of ^{56}Ni produced also varied with metallicity (Bravo et al. 2010; Jackson et al. 2010). DDT models with varying metallicity and fixed detonation density, however, showed little variation in outcome (Townsley et al. 2009).

The authors wish to acknowledge that this work was supported by the US Department of Energy, Office of Nuclear Physics, under contract DE-AC02-06CH11357. This work was also supported by the NSF, grant AST-0507456, by the **J**oint **I**nstitute for **N**uclear **A**strophysics at MSU under NSF-PFC grant PHY 0822648, by the DOE through grant 08ER41570, and by the Deutsche Forschungsgemeinschaft via the Emmy Noether Program (RO 3676/1-1). The software used in this work was in part developed by the DOE-supported ASC / Alliance Center for Astrophysical Thermonuclear Flashes at the University of Chicago. Simulations presented in this work were run at the High Performance Computing Center at Michigan State University.

REFERENCES

Bravo, E., Domínguez, I., Badenes, C., Piersanti, L., & Straniero, O. 2010, ApJ, 711, L66
Caughlan, G. R. & Fowler, W. A. 1988, At. Data Nucl. Data Tables, 40, 283
Chamulak, D. A., Brown, E. F., & Timmes, F. X. 2007, ApJ, 655, L93
Chamulak, D. A., Brown, E. F., Timmes, F. X., & Dupczak, K. 2008, ApJ, 677, 160
Cyburt, R. H., Amthor, A. M., Ferguson, R., Meisel, Z., Smith, K., Warren, S., Heger, A., Hoffman, R. D., Rauscher, T., Sakharuk, A., Schatz, H., Thielemann, F. K., & Wiescher, M. 2010, ApJS, 189, 240
Fink, M., Röpke, F. K., Hillebrandt, W., Seitenzahl, I. R., Sim, S. A., & Kromer, M. 2010, A&A, 514, A53+
Fryxell, B., Olson, K., Ricker, P., Timmes, F. X., Zingale, M., Lamb, D. Q., MacNeice, P., Rosner, R., Truran, J. W., & Tufo, H. 2000, ApJS, 131, 273
Fuller, G. M., Fowler, W. A., & Newman, M. J. 1982, ApJS, 48, 279
Gamezo, V. N., Khokhlov, A. M., & Oran, E. S. 2004, Phys. Rev. Lett., 92, 211102
Graboske, H. C., Dewitt, H. E., Grossman, A. S., & Cooper, M. S. 1973, ApJ, 181, 457
Hillebrandt, W. & Niemeyer, J. C. 2000, ARA&A, 38, 191
Hillebrandt, W., Sim, S. A., & Röpke, F. K. 2007, A&A, 465, L17
Iliadis, C., D'Auria, J. M., Starrfield, S., Thompson, W. J., & Wiescher, M. 2001, ApJS, 134, 151
Jackson, A. P., Calder, A. C., Townsley, D. M., Chamulak, D. A., Brown, E. F., & Timmes, F. X. 2010, ApJ, 720, 99
Kasen, D. & Plewa, T. 2005, ApJ, 622, L41
—. 2007, ApJ, 662, 459
Khokhlov, A. M. 1983, Soviet Astronomy Letters, 9, 160
—. 1991, A&A, 245, 114
Kromer, M., Sim, S. A., Fink, M., Röpke, F. K., Seitenzahl, I. R., & Hillebrandt, W. 2010, ApJ, 719, 1067
Langanke, K. & Martínez-Pinedo, G. 2001, At. Data Nucl. Data Tables, 79, 1
Livne, E., Asida, S. M., & Höflich, P. 2005, ApJ, 632, 443
Maeda, K., Benetti, S., Stritzinger, M., Röpke, F. K., Folatelli, G., Sollerman, J., Taubenberger, S., Nomoto, K., Leloudas, G., Hamuy, M., Tanaka, M., Mazzali, P. A., & Elias-Rosa, N. 2010, Nature, 466, 82
Mazzali, P. A., Röpke, F. K., Benetti, S., & Hillebrandt, W. 2007, Science, 315, 825
Meakin, C. A., Seitenzahl, I., Townsley, D., Jordan, G. C., Truran, J., & Lamb, D. 2009, ApJ, 693, 1188
Plewa, T. 2007, ApJ, 657, 942
Plewa, T., Calder, A. C., & Lamb, D. Q. 2004, ApJ, 612, L37
Reinecke, M., Hillebrandt, W., & Niemeyer, J. C. 2002, A&A, 391, 1167
Röpke, F. K., Hillebrandt, W., Schmidt, W., Niemeyer, J. C., Blinnikov, S. I., & Mazzali, P. A. 2007a, ApJ, 668, 1132
Röpke, F. K., Woosley, S. E., & Hillebrandt, W. 2007b, ApJ, 660, 1344
Seitenzahl, I. R., Meakin, C. A., Lamb, D. Q., & Truran, J. W. 2009a, ApJ, 700, 642
Seitenzahl, I. R., Meakin, C. A., Townsley, D. M., Lamb, D. Q., & Truran, J. W. 2009b, ApJ, 696, 515
Sim, S. A., Röpke, F. K., Hillebrandt, W., Kromer, M., Pakmor, R., Fink, M., Ruiter, A. J., & Seitenzahl, I. R. 2010, ApJ, 714, L52
Sim, S. A., Sauer, D. N., Röpke, F. K., & Hillebrandt, W. 2007, MNRAS, 378, 2
Townsley, D. M., Jackson, A. P., Calder, A. C., Chamulak, D. A., Brown, E. F., & Timmes, F. X. 2009, ApJ, 701, 1582
Woosley, S. E., Arnett, W. D., & Clayton, D. D. 1973, ApJS, 26, 231
Woosley, S. E. & Weaver, T. A. 1994, ApJ, 423, 371